A STUDY OF THE INFLUENCE OF CROSS FLOW ON THE BEHAVIOR OF AIRCRAFT WAKE VORTICES NEAR THE GROUND

Z. C. Zheng*, R. L. Ash**
Department of Aerospace Engineering
Old Dominion University
Norfolk, VA23529
G. C. Greene†
NASA Langley Research Center
Hampton, VA23681

Abstract

This paper has studied the influence of cross wind on a vortex pair interacting with the ground. The study has been focused on exploring how various types of cross flow alter the trajectories and strengths of each vortex in different laminar ambient flows. The computation has employed the vorticity-streamfunction formulation of the Navier-Stokes equations. Then, the computational results have been used to determine downwash velocities and induced rolling moment on hypothetical following aircraft, employing Prandtl's lifting line theory. This method provides alternative means to assess the wake vortex hazard.

Introduction

Aircraft wake encounters can cause serious loss of control problems for following aircraft. The hazard is more severe near airports, because of the limited time and space available to recover from an upset when the affected aircraft are close to the ground. Airports with multiple runways present special difficulties, because cross winds can alter the trajectories and lifetimes of these wake vortices (Burnham *et al.*[1]), causing them to persist in adjacent flight paths. Improved forecasting techniques can result in safer airport operations and permit higher passenger throughput. The work reported here is directed toward that end by improving wake vortex simulation capabilities.

Previously, a two-dimensional, numerical/theoretical model of a trailing line vortex pair near the ground was developed which could simulate the behavior of aircraft wakes with atmospheric effects (Zheng and Ash[2,3]). The model utilized a vorticity-streamfunction formulation of the Navier-Stokes equations, incorporating a modified Boussinesq approximation to account for density stratification and thus permit simulation of the descent of a vortex pair in close proximity with the ground. Numerical simulations of laminar, unstratified vortex descent were found to be in good agreement with the laboratory experiments of Liu and Srnsky[4]. The simulations showed that vortex rebound near the ground was caused by the separation of the ground-plane boundary layer, in agreement with the widely accepted rebound scenario described by Harvey and Perry[5].

When a cross wind is present, the atmospheric shear vorticity causes asymmetry in the wake flow field. Aircraft flight tests have shown that when smoke is introduced into the vortex system, one of the two primary trailing vortices can vanish while the second smoke trail remains intact (see Burnham *et al.*[1]). Numerical calculations reported by Rossow[6] and Bilanin, Teske and Hirsh[7] demonstrated that the primary vortex which rotated with the same rotational sense as the shear gradient existed for longer time intervals than the vortex of opposite rotational sign, which was distorted more rapidly. In addition, the measurements of Burnham *et al.*[1] exhibited vortex tilting phenomena, where the initially symmetric vortex pair rotated away from its perpendicular (to the ground plane) symmetry plane.

An unanswered question was: Why does the upwind vortex sometimes appear to rise relative to the downwind vortex, while at other times the opposite rotation seems to occur (see Donaldson and Bilanin[8])? If atmospheric shear is constant and the wake is not in ground effect, a closed form solution, based on potential flow approximations was found by Lissaman *et al.*[9]. For this ideal solution, even with wind shear, the two vortices were found to descend at their classical rates, $|v| = \Gamma/4\pi s_0$, where Γ is the circulation and s_0 is the half-span of the vortex pair. The inviscid model displayed no tendencies for the vortex pair to tip or tilt. The effect of a ground plane on the ideal solution was considered by Brashears, Logan and Hallock[10] . They studied the upwelling of streamlines by considering the stagnation point positions. The location of the uppermost stagnation point (of the two stagnation points in the flow field), caused by the interaction between crosswind shear and the vortex pair, correlated with sys-

* Research Associate, Member of AIAA
** Professor, Associate Fellow of AIAA
† Senior Research Engineer, Associate Fellow of AIAA

tem rotation trends. That is, the vortex with the higher stagnation point was observed to rise more. However, the approximate solution did not actually predict the tilting phenomenon. The results showed that weak vertical shear can cause the downwind vortex to rise more rapidly than the upwind vortex and that strong vertical shear will have the opposite effect. The results of Delisi, Robins and Fraser[11] for stable stratification with and without ground effect showed the same trends. Their ground effect results also showed that vertical shear reduced the rebound when compared with non-sheared flows.

A numerical scheme, extended from Zheng and Ash[2, 3] has been used to predict crosswind effects on vortex wake behavior near the ground for both laminar and turbulent wake vortex flows. Moving grids were required in order to capture the vortex pair propagating with cross flow convection. At this stage of the study, a uniformly moving grid, with constant translational speed, U_g, equal to the estimated translational velocity of the centroid of the vortex pair, has been used to capture the crosswind flow field. The uniformly moving grid gives proper resolution within the period of vortex sustenance, for typical atmospheric crosswind profiles. However, we will show that the vorticity-streamfunction formulation, under any type of time dependent translational coordinate motion, with velocity components $U_g(t)$ and $V_g(t)$, is not affected by the unsteady motion. Rather, the crosswind convection effects are only observed in the boundary conditions.

In this paper, only the laminar, unstratified cases are presented. The wake vortex trajectories resulting from representative crosswind profiles have been calculated. This work has concentrated on revealing the mechanisms that produce tilting of the vortex pair near the ground. In addition, the vortex hazard around the core regions of each vortex (in the vortex pair) has been quantified using Prandtl's lifting line theory, to estimate the induced rolling moment on following aircraft.

Formulation in Moving Coordinates

The coordinate system for this unsteady, two-dimensional incompressible problem is shown in Figure 1, which is assumed fixed with respect to the ground. The vorticity-streamfunction formulation can be employed to eliminate one variable (pressure) in the two-dimensional governing equations. The dimensionless form of the vorticity-transport equation is given by:

$$\frac{D\zeta}{Dt} = \frac{1}{Re}\nabla^2\zeta, \tag{1}$$

where

$$\zeta = \frac{\partial v}{\partial x} - \frac{\partial u}{\partial y}. \tag{2}$$

Using the initial vortex half-span, s_0, as the characteristic length, and the initial circulation, Γ_0, a flow Reynolds number can be defined as:

$$Re = \Gamma_0/\nu_o\,, \tag{3}$$

and a characteristic velocity and time can be given by Γ_0/s_0 and s_0^2/Γ_0, respectively. From the incompressibility condition, the streamfunction equation,

$$\nabla^2\psi = -\zeta\,, \tag{4}$$

applies, where

$$u = \frac{\partial\psi}{\partial y}, \quad \text{and} \quad v = -\frac{\partial\psi}{\partial x}\,. \tag{5}$$

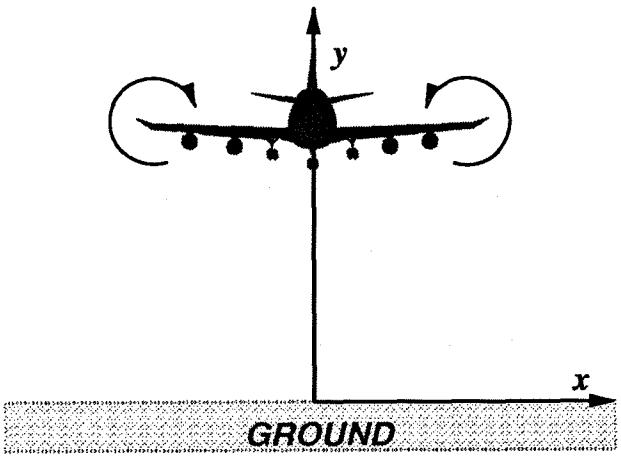

Figure 1 Coordinate systems used in this study

However, under the influence of the cross wind, the vortex pair convects with the cross flow and a moving coordinate system must be used in order to retain the vortex pair within the computational grid. For a rigorous proof that time dependent uniform grid motions do not alter the governing equations, we start with the primitive variable conservation of momentum equations. Appending the variables in the space-fixed coordinate system with a subscript, f, the dimensionless two-dimensional momentum equations are

$$\frac{\partial u_f}{\partial t_f} + u_f\frac{\partial u_f}{\partial x_f} + v_f\frac{\partial u_f}{\partial y_f} = -\frac{\partial p_f}{\partial x_f} + \frac{1}{Re}\nabla_f^2 u_f\,, \tag{6}$$

and

$$\frac{\partial v_f}{\partial t_f} + v_f\frac{\partial v_f}{\partial x_f} + v_f\frac{\partial v_f}{\partial y_f} = -\frac{\partial p_f}{\partial y_f} + \frac{1}{Re}\nabla_f^2 v_f\,. \tag{7}$$

We can transfer this system from the space fixed coordinates to non-inertial, translational moving-coordinates where the translational velocity components are $U_g(t)$ and $V_g(t)$, using the relations:

$$\frac{\partial}{\partial x_f} = \frac{\partial}{\partial x}\,, \tag{8}$$

$$\frac{\partial}{\partial y_f} = \frac{\partial}{\partial y}\,, \tag{9}$$

$$\frac{\partial}{\partial t_f} = \frac{\partial}{\partial t} - U_g(t)\frac{\partial}{\partial x} - V_g(t)\frac{\partial}{\partial y}\,, \qquad (10)$$

so that the conservation of momentum equations become

$$\frac{\partial u_f}{\partial t} + (u_f - U_g)\frac{\partial u_f}{\partial x} + (v_f - V_g)\frac{\partial u_f}{\partial y} = -\frac{\partial p_f}{\partial x} + \frac{1}{Re}\nabla^2 u_f\,, \qquad (11)$$

and

$$\frac{\partial v_f}{\partial t} + (u_f - U_g)\frac{\partial v_f}{\partial x} + (v_f - V_g)\frac{\partial v_f}{\partial y} = -\frac{\partial p_f}{\partial y} + \frac{1}{Re}\nabla^2 v_f\,, \qquad (12)$$

respectively. Since the thermodynamic pressure is not affected by coordinate motion, we know that

$$p = p_f\,, \qquad (13)$$

and the velocity components in the moving coordinates are related to the space fixed coordinates by

$$u = u_f - U_g \text{ and } v = v_f - V_g\,. \qquad (14)$$

Eqns. (11) and (12) can thus be rewritten as

$$\frac{\partial u}{\partial t} + \frac{dU_g}{dt} + u\frac{\partial u}{\partial x} + v\frac{\partial u}{\partial y} = -\frac{\partial p}{\partial x} + \frac{1}{Re}\nabla^2 u\,, \qquad (15)$$

and

$$\frac{\partial v}{\partial t} + \frac{dV_g}{dt} + u\frac{\partial v}{\partial x} + v\frac{\partial v}{\partial y} = -\frac{\partial p}{\partial y} + \frac{1}{Re}\nabla^2 v\,. \qquad (16)$$

In Eqns. (15) and (16), it can be seen that extra terms have been produced by the transformation of Eqns. (8)-(10), representing the accelerations of the moving frame. However, since U_g and V_g are functions only of time, cross differentiation of Eqns. (15) and (16) to form the vorticity transport equation yields the original, unconvected version of Eqn. (1).

In deriving the vorticity transport equation, the solenoidal relation for the velocity field in moving coordinates has been used. Mathematically, it can be observed from Eqn. (14) that the spatial derivatives in the transformed coordinates agree with the expressions in fixed coordinates and thus the solenoidal relation is not altered. Physically, the incompressibility of the flow field cannot be changed by the moving frame of reference. Hence, the streamfunction equation, which is based on the solenoidal velocity requirement, is the same as Eqn. (4), if we define

$$\frac{\partial \psi}{\partial y} = u_f - U_\infty \equiv u\,, \qquad (17)$$

and

$$\frac{\partial \psi}{\partial x} = -(v_f - V_\infty) \equiv -v\,. \qquad (18)$$

From the above procedures, we see that this transformation is "transparent" in that it does not alter the vorticity-streamfunction formulation; however, it is not transparent for primitive variable formulations in two-dimensional flows. The additional terms, produced by the translational acceleration, must be retained in the momentum equations. As stated previously, when the cross derivatives are employed to develop the vorticity transport equation, the translational acceleration terms, which must be irrotational, vanish. This case can be considered as a special case of Speziale's[12] three-dimensional vorticity-velocity formulation for a non-inertial frame of reference.

Since crosswind effects cause lateral direction shifts of the vortex system, a moving grid is required only in the x-direction, with V_g equal to zero. The ideal case is to set U_g exactly equal to the lateral velocity of the centroid of the vortex pair. However, the additional computational effort required for precise tracking of the centroid is not justified if the required resolution can be achieved using simpler methods. In the following simulations, we have found that the imposed crosswind speed at the vertical elevation, $y = 1.5$, can be used to characterize the convection speed of the vortex pair; using that velocity as the grid convection speed, we have found that both vortices stay in the required high resolution grid regions. The (150×300) grid used previously in the first quadrant for a symmetric vortex system (Zheng and Ash [2]), and which employed an exponential transformation to map the finite computational domain to an infinite region, was reflected into the second quadrant to form a (300×300) network for the asymmetric simulations. The high density grid regions were therefore maintained within close proximity of the convected vortex trajectories during the wall encounter phase.

Influence of Crosswind Profiles

The following cases have been simulated at a vortex Reynolds number of 1,000. The computational scheme developed by Zheng and Ash [2] has been employed, with upwind differencing applied on the convection terms and central differencing on the diffusion terms in Eqn. (1). The Poisson solver developed by Swartztrauber and Sweet[13] has been used to integrate Eqn. (2). The computation has been performed on the Cray 2 and Cray Y-MP computers at NASA Langley Research Center. A typical case utilized 10 mega-words for run time memory and required approximately 6 hours of CPU time on the Cray Y-MP computer.

Crosswind velocity distributions were combined with the asymptotic representations, developed in Zheng and Ash [2], for the vortex system during flow field initialization. Assuming the vorticity and streamfunction of the crosswind are ζ_c and ψ_c, where

$$\nabla^2 \psi_c = -\zeta_c\,, \qquad (19)$$

the solutions from the asymptotic initialization method have the same relationship; that is,

$$\nabla^2\psi_a = -\zeta_a \ . \tag{20}$$

Hence, the combined initial vorticity and streamfunction distributions must be given by:

$$\zeta_i = \zeta_c + \zeta_a \ , \ \psi_i = \psi_c + \psi_a \ , \tag{21}$$

thus satisfying the kinematic relationship between the initial vorticity and streamfunction,

$$\nabla^2\psi_i = -\zeta_i \ . \tag{22}$$

In addition, crosswind velocity distributions were also imposed as inflow and outflow boundary conditions (at $x = \pm\infty$) for all subsequent times.

We first tested cross-flow velocity profiles with von Karman's integral representation for laminar boundary layers, where:

$$u_c(x,y)/U_\infty = \begin{cases} 2\left(\frac{y}{\delta}\right) - 2\left(\frac{y}{\delta}\right)^3 + \left(\frac{y}{\delta}\right)^4 \\ \qquad\qquad for\ y \le \delta \\ 1 \qquad\qquad for\ y > \delta \end{cases} \ . \tag{23}$$

In Figure 2, the trajectories of both vortices have been plotted for various thick cross flow boundary layers, with δ = 10 and far-field dimensionless velocities of U_∞ = 0.05 (slow), U_∞ = 0.1 (moderate) and U_∞ = 0.5 (fast). The trajectory behavior for a thin boundary layer (δ = 1), with a moderate cross flow velocity (U_∞ = 0.1) is shown in Figure 3. The thick cross-flow boundary layer cases can also be considered to represent cases when the vortex pair is traversing through a constant shear flow, since the crosswind velocity profile in the region containing the vortex pair approximates a constant gradient. The thin cross-flow boundary case represents a flow system where the crosswind velocity is approximately uniform near the vortex pair, but the crosswind profile generates significant vorticity close to the ground. It is noted that the trajectories in Figures 2 and 3 were simulated for a total dimensionless time interval of t_{max} = 60, and the time histories can be deduced from the trajectories, using the "+" symbols which locate the vortex centers at dimensionless time increments of 10.

For the left-hand (upstream) vortex, the cross flow can compensate for the lateral motion produced by the vortex-ground encounter so that the vortex can become almost stationary, as represented by the case shown in Figure 2, when U_∞ = 0.1. When the cross-flow velocity is increased significantly (U_∞ = 0.5), both the upstream vortex and the downstream vortex are driven downstream by the fast-moving cross flow; obviously, the downstream vortex is being convected more rapidly to the right in all the cases. In Figure 2, while the right-hand vortex stays slightly farther from the wall than the left-hand vortex in the slow cross-flow case, the right-hand or downstream vortex traverses a path which is substantially farther from the wall in the moderate and fast cross-flow cases.

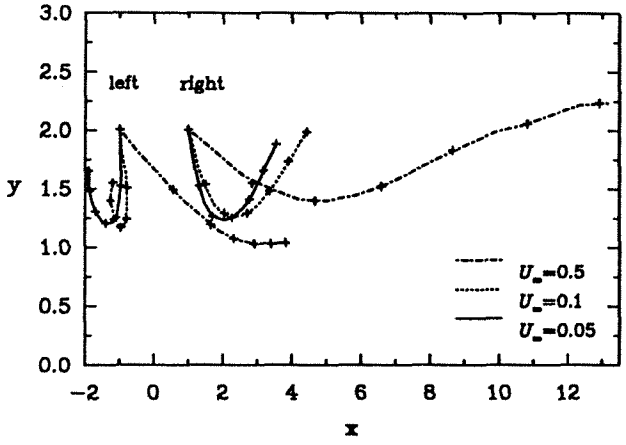

Figure 2 Influence of cross flow on vortex pair trajectories at Re=1,000, δ=10, with various U_∞

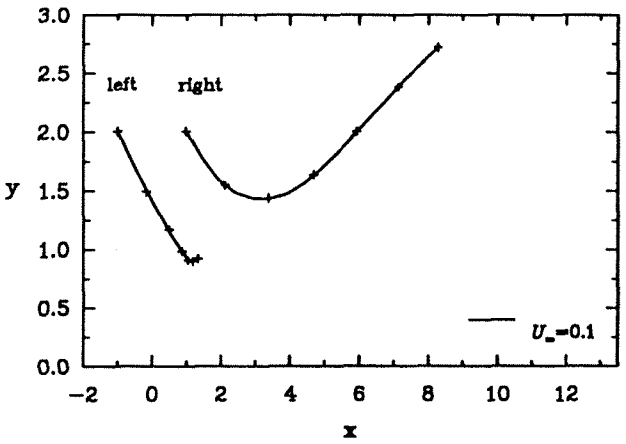

Figure 3 Influence of cross flow on vortex pair trajectories at Re=1,000, δ=1, with U_∞=0.1

The vortex trajectory trends exhibited in Figure 2 can be explained on the basis of the additional vorticity generated by the cross-flow boundary layer. Since the vorticity produced by the cross-flow boundary layer has the same sign as the vorticity induced along the wall by the downstream vortex, a thicker viscous region is established beneath the downstream vortex than would occur in the quiescent ambient case. A corresponding thinning of the viscous region occurs beneath the upstream vortex, because the superimposed vorticities are of opposite sign. As a result, the separated flow region beneath the downstream vortex is larger and the opposite sign, secondary vortex is stronger, thereby acting more vigorously to displace that vortex away from the wall. Since an increase in the magnitude of the cross-flow boundary layer (with the same thickness) generates additional vorticity, the influence of the cross flow boundary layer on the downstream vortex trajectory becomes more pronounced with increased speed. The vorticity contours for

$\delta = 10$, $U_\infty = 0.1$, shown in Figure 4, show the evolution of the vorticity field at an early encounter time and at a post-rebound time. It should be noted that because the secondary vortex interactions start when the vortex pair is close to the ground, the two primary vortices have nearly the same vertical descent histories before vortex rebound is initiated. When vortex rebound starts, the right vortex elevation history begins to deviate from that of the left vortex because of the significant differences which then exist between the two secondary vortices.

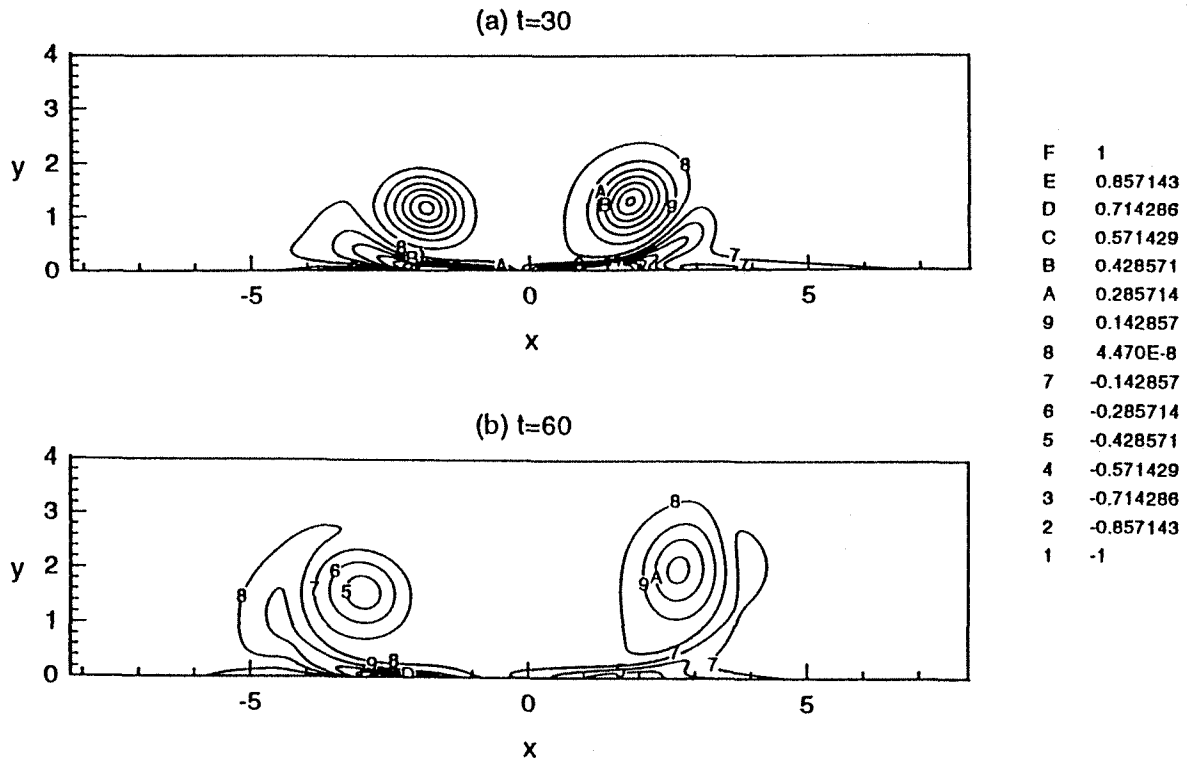

Figure 4 Vorticity contours for Re=1,000, δ=10, U_∞ = 0.1. (a) t=30; (b) t=60. (The coordinate system in this figure moves at the lateral speed U_g = 0.03)

The thin cross-flow boundary layer (Figure 3) carries stronger vorticity concentrated near the ground, when compared with a thick cross-flow boundary layer with the same U_∞ (0.1, Figure 2). Figure 3 shows that the counterclockwise tilting of the vortex pair is stronger than the case in Figure 2. Comparing the U_∞ =0.1 cases in Figures 2 and 3, it can be seen how the additional vorticity generated by the cross wind boundary layer influences the vortex trajectories very strongly. Even though the vortices are immersed in a strong shear flow when δ = 10 (Figure 2), vorticity production at the wall is an order of magnitude smaller in that case than when δ = 1 (Figure 3). The higher levels of vorticity under the vortices for the δ = 1 case alters the size and strength of the newly-formed secondary vortices significantly, resulting in greater tilting. An interesting phenomenon in Figure 3 is the fact that the upstream vortex becomes stationary near the ground, at the later time stages. It neither rebounds nor propagates in the lateral direction. The induced ground boundary layer under it, which causes the rebound, is cancelled completely by the cross-flow boundary layer, while the lateral motion, caused by the vortex interacting with the ground plane, is balanced by the advection of the cross flow. This situation can be very hazardous for airports with parallel runways, since the upstream vortex can hover near the ground on an adjacent runway while it decays slowly.

In field observations, the vortex pair is sometimes observed to rotate in the opposite direction to the cases described previously. The crosswind direction relative to the observer (i.e. from right to left instead of from left to right), of course, changes the vortex pair rotation direction. But that does not change the previous explanation, if the terms "upstream" and "downstream" vortices are used. That is, clockwise rotations have been observed for left to right cross winds. It is noted that in all the cases shown in Figures 2 and 3, the crosswind only produces negative sign vorticity, but that is not always the case in atmospheric boundary layers. In fact, crosswind velocity profiles can exhibit complex shapes (e.g. Lee and Black[14]), generating both positive and negative vorticity in local regions. Hence, we have tested cases with crosswind profiles of types shown in Figure 5, which contains a "ground jet". The vorticity in this type of velocity profile is negative very close to the ground, then becomes positive before it returns to zero away from the ground.

The expression used for representing this velocity profiles was:

$$u_c(x,y)/U_s = \frac{y}{1+(y/\beta)^4} \qquad (24)$$

where U_s controls the strength of the crosswind and β determines the position of the maximum velocity. The test cases have been run for U_s = 0.1 and U_s = 0.5, respectively, with β = 0.33. Figure 5 shows the crosswind velocity profile for U_s = 0.1.

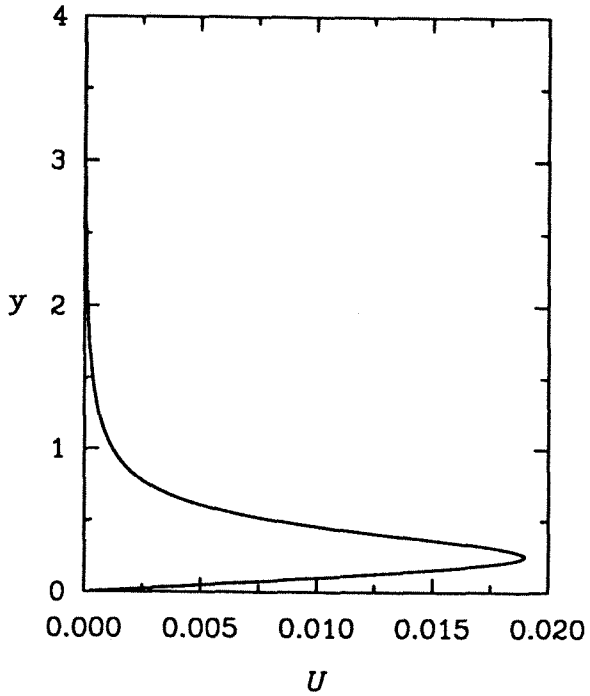

Figure 5 "Ground jet" type crosswind velocity profile for U_s = 0.1, β = 0.33

Figure 6 shows the trajectories for both jetting cases, for a total simulation time of 60 and the time marks are again in 10 unit increments. The U_s = 0.5 case shows that the upstream (left-side) vortex rebounds very quickly and is always farther away from the ground plane than the downstream vortex. The clockwise rotation of the vortex pair is also shown in the U_s = 0.1 case. In that case, the downstream vortex elevation, after rebound, catches up with the upstream vortex near the end of the simulation. The trajectories in Figure 6 can be explained using the vorticity contours in Figure 7 corresponding to the U_s = 0.5 case. The ground boundary-layer effects resulting from the cross-flow vorticity production still exist in the region very close to the ground, since the crosswind retains its negative sign vorticity in that region and the secondary vortex mechanism, explained previously, applies. However, a little farther from the ground, the crosswind possesses positive sign vorticity and the positive sign vorticity layer obviously causes a clockwise rotation of the vortex pair, in the same manner as its negative vorticity counterpart (which was the only mechanism for the von Karman type crosswind profiles). Since the positive vorticity layer is closer to the vortex pair than the negative vorticity layer in the cross-flow profiles, it exerts a stronger influence on the vortex pair initially. After the significant secondary vortex is generated underneath the downstream vortex, in the U_s = 0.1 case, the negative vorticity effects gradually become balanced with the effects from the positive vorticity and thus the downstream vortex ultimately reaches about the same elevation as the upstream vortex at the end of the simulation.

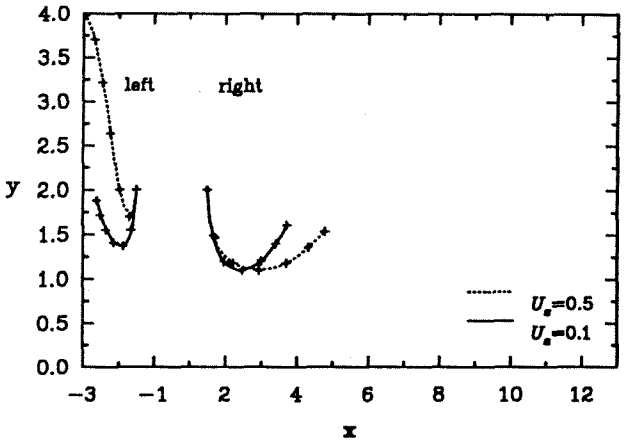

Figure 6 Influence of "ground jet" type cross wind on vortex pair trajectories at Re=1,000, β=0.33, with various U_s

The Vortex Hazard Assessment

In order to assess the vortex hazard, some measure of hazard strength is required. However, since the computational domain is an unbounded quadrant, overall or global measures of circulation or velocity levels are of little value. The *approach zone* method used in Zheng and Ash[2] could be meaningful in some sense. In that earlier work, circulation and kinetic energy were calculated in a bounded zone, which was assumed to represent the runway flight domain. However, the definition of the approach zone was somewhat arbitrary and neither circulation nor kinetic energy were direct measures of the vortex hazard. Therefore, a more systematic method was developed during this study. The rolling moment, induced on a following aircraft by the wake vortex flow from a leading aircraft, has been used as a measure to assess the hazard.

In the rolling moment method, the downwash velocity field, produced computationally by the numerical scheme introduced above, is utilized with a simplistic following aircraft model. The following aircraft was represented two-dimensionally as a flat-plate rectangular wing. In the current model, the influence of the following aircraft on the upstream flow field is neglected (Stewart[15]), as is the thickness of the following aircraft wings. In addition, any bank angles produced by the rolling motion

of the following aircraft are neglected. Indeed, the calculated rolling moment should be indicative of the control authority required by the following aircraft to prevent large angle rolls. Then, employing Prandtl's lifting line theory (Karamcheti[16] and Bertin and Smith[17]), the induced rolling moment coefficient can be obtained using Fourier series expansions.

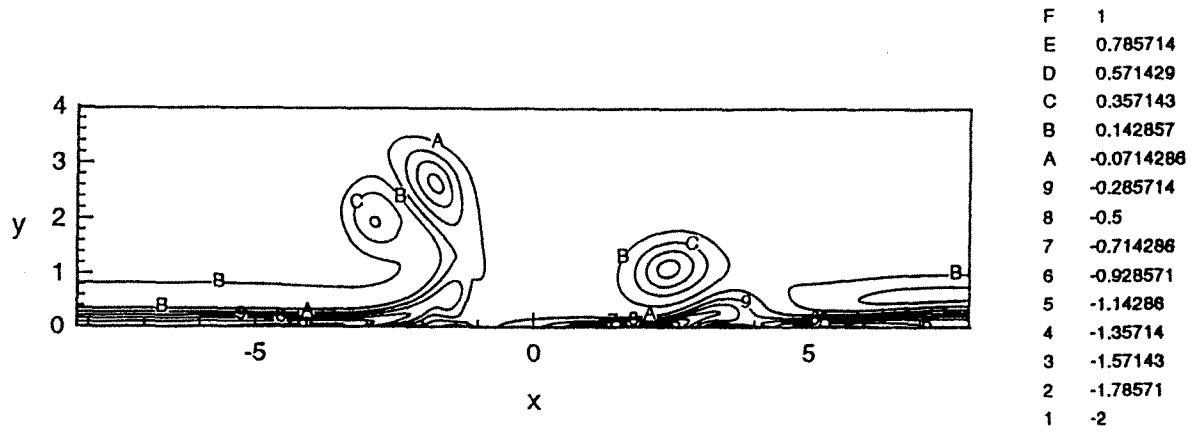

Figure 7 Vorticity contours of the vortex pair under the influence of the "ground jet" type crosswind, with $U_s = 0.5$. (The coordinate system in this figure moves at the lateral speed $U_g = 0.0018$)

Consider a spanwise circulation distribution on the following wing that can be represented by a Fourier sine series consisting of N terms:

$$\Gamma(\theta) = 4sW_\infty \sum_1^N A_n sin(n\theta) \,, \qquad (25)$$

where s is the half-span of the following airplane, W_∞ is its forward speed (in the z-direction, in the coordinate system employed here) and θ is used to replace the physical spanwise coordinate of the "following aircraft", $\hat{x}$, defined as:

$$cos\theta = -\frac{\hat{x}}{s} \,, \quad -1 \le \frac{\hat{x}}{s} \le 1 \,. \qquad (26)$$

The unit lift force, acting on that spanwise section for which the circulation is $\Gamma(\theta)$, is given by

$$l(\theta) = \rho_\infty W_\infty \Gamma(\theta) = 4\rho_\infty s W_\infty^2 \sum_1^N A_n sin(n\theta) \,. \quad (27)$$

The rolling moment on the wing then can be expressed by:

$$M_r = \frac{1}{2}s^2 \int_0^\pi l(\theta) sin(2\theta) d\theta = \pi \rho_\infty W_\infty^2 s^3 A_2 \,, \quad (28)$$

and the rolling moment coefficient is:

$$C_l = \frac{\pi}{4}(AR)\ A_2 \qquad (29)$$

where (AR) represents the aspect ratio of the wing. Hence, it has been shown that in order to get the rolling moment coefficient for a certain type of following aircraft (wings), only the second coefficient in the Fourier sine expansion must be calculated. Now, we have for the down wash velocity:

$$v(\hat{x}) = \frac{1}{4\pi} \int_0^\pi \frac{d\Gamma/dx^*}{x^* - \hat{x}} dx^* = W_\infty \frac{\sum_1^N nA_n sin(n\theta)}{sin\theta} \qquad (30)$$

and if we can perform a Fourier sine expansion on v, which is calculated from the Navier-Stokes calculation using Eqn. (5), we can obtain the rolling moment coefficient easily. In the following examples, the calculated rolling moment coefficient is actually the second coefficient in the Fourier series, A_2, and the vertical velocity component, computed from Eqn. (5), is used as the downwash, v/W_∞, so that the presented result can be used with various following aircraft types and different approaching speeds.

An example without cross flow effects, is shown in Figure 8, with the same Reynolds number Re = 1,000, where the "following airplane" has the same wing span as the generating airplane. Since the flow field is symmetric in this case, only half of the domain is displayed. The contours show the rolling moment coefficient at each point for this particular size of following airplane, assuming its center is flying through that point in space. This representation shows that when the following airplane is flying near the region occupied by the vortex core, the rolling moment is large (negative sign) and therefore the hazard is more significant. When the follower moves laterally away from the vortex center, the rolling moment becomes smaller. Further lateral displacement to a position where only one side of the follower wing is influenced by the vortex, results in a sign change for the

induced rolling moment, which is obviously true physically. Figure 9 explains pictorially such sign changes in relation to the position of the follower. It is noted further that the maximum positive rolling moment is much smaller than the largest negative value, allowing us to conclude that the most hazardous region is the region around each vortex core.

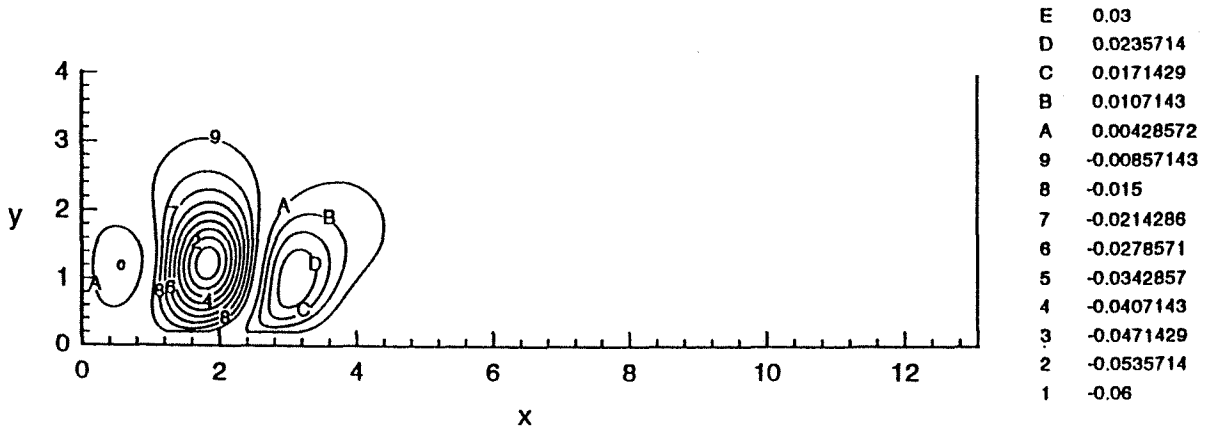

Figure 8 Contours of the rolling moment coefficient for the case without crosswind effects, with the same size follower, at t = 30

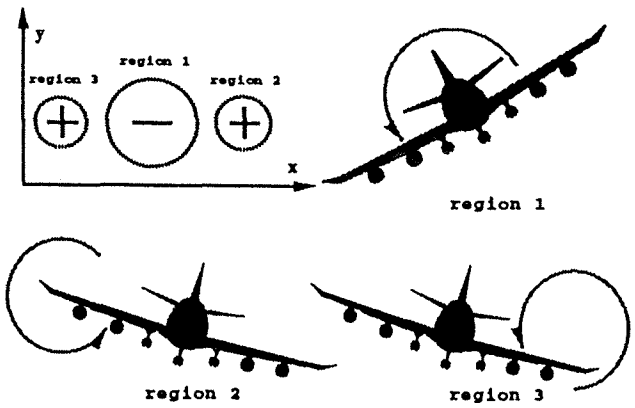

Figure 9 Illustration of the sign change of the rolling moment coefficient when the follower is at different positions

The time history of the rolling moment coefficient at the vortex core is shown in Figure 10, comparing the decay of the rolling moment coefficients for two different follower wing spans. It can be seen that initially the induced rolling moment coefficient is larger for the smaller follower, and then it decays faster than that for the larger follower. That is because the vortex core is small initially, and both the small and large followers are then subjected to the same levels of induced circulation around the vortex core region, resulting in a larger rolling moment coefficient on the small follower in that region. After the vortex core has dilated, its core size can become comparable with the span of the small follower. However, most of the circulation can still contribute to the large size follower, while the small follower loses some of the rolling energy induced by the vortex. That of course does not mean that a smaller follower is safer than a larger follower. Since a large follower has more control capacity to sustain and recover from the roll upset. Second, in this study a very low Reynolds number is considered, which is about three orders of magnitude smaller than the Reynolds number in actual flight cases (10^6 to 10^7). Therefore, in real cases, the vortex core decays much slower than the case studied here and a small follower is subjected to greater risk when flying through a region close to the vortex core. This is additional evidence which shows that it is very important to reduce vortex core diffusion in computational predictions in order to avoid underestimating the vortex hazard.

On the other hand, since the vortex core dilation should not have significant effect on the large size followers, the core dilation due to the low Reynolds number calculation has much less influence on the time decay of rolling moment for the $s = 1$ case. Hence, the results have shown that the hazard is predicted to decrease quickly for aircraft similar in size to the wake generating aircraft.

The cross-flow effects on the rolling moment have been shown for the case with $\delta = 10$, $U_\infty = 0.5$ in a von Karman type cross-flow profile (Figure 11, for the same size follower and generator). It has been noted that this case resembles strong constant shear around the vortex pair and therefore causes significant asymmetry effects on the vortex system. In this case, the vorticity at the center of the upstream vortex, which has the same sign as the wind shear, decays more slowly than that at the downstream vortex. However, the rolling moment coefficient histories at the centers of the two vortices, plotted in Figure12 and Figure 13, are very similar. Again, the smaller follower (half of the generator) case is plotted for

comparison and the same decay pattern, as in the symmetric case, is shown.

Rossow (1994)[18] used a vortex lattice method to compute the loads induced on aircraft, using measured downwash velocities from vortex wakes produced in the 80– by 120–foot wind tunnel at NASA Ames Research Center. Comparison of the computed results with the measured lift and rolling moment distributions was made in his study. Since the Reynolds number and some other flow parameters are different in this paper, comparison with his experimental data cannot be used directly to validate the current method. Validation of the hazard assessment method, as well as the computational simulation of vortex wakes, will certainly be pursued in future research. In addition, a parametric study, considering various cross-flow velocity profiles and following aircraft, is in progress.

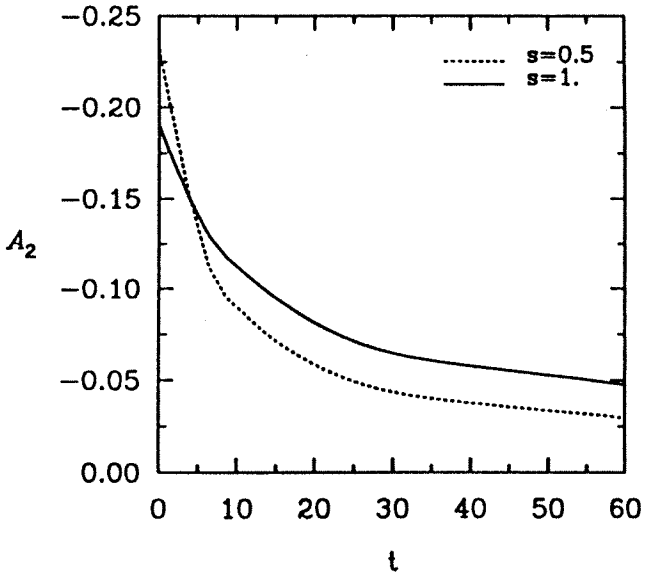

Figure 10 Rolling moment coefficient history at the center of the vortex, without crosswind effects

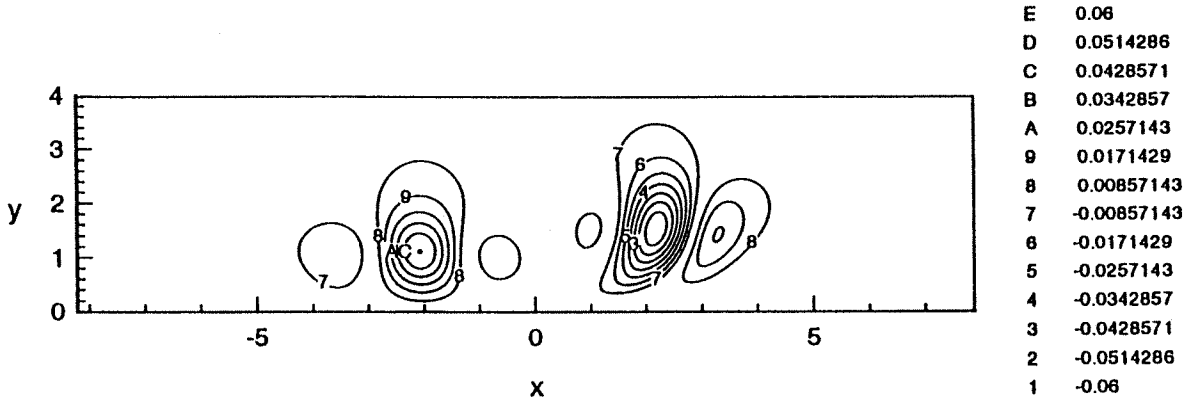

Figure 11 Contours of rolling moment coefficient for the case with crosswind influence, with δ=10, U_∞=0.5, at t=30. (The coordinate system in this figure moves at the lateral speed U_g = 0.15)

Conclusions

This research has shown how a wake vortex pair can interact with the ground for a range of cross wind conditions. For simple laminar boundary-layer type crosswind velocities, the vortex pair rotates into the cross wind, in the sense that the downwind vortex rebounds higher than the upwind vortex. The extent of these asymmetric rotations is stronger when the cross wind vorticity production along the ground plane is larger. When cross wind velocity profiles are more complex, which is often the case for local planetary boundary layers, the vortex system can rotate in either direction. Specifically, when nocturnal- or ground-jet-type cross wind profiles are present, the opposite sign vorticity associated with the jet region causes the vortex pair to rotate away from the cross wind.

A method to assess the vortex hazard has been developed, which used the computational results as downwash to calculate rolling moment coefficients induced on following aircraft. The result has shown that the regions with strongest induced rolling moment are near the vortex core. The estimated rolling moment coefficients vary for different following aircraft types. The smaller follower retains a larger rolling moment coefficient at the vortex center initially, but the loads decay faster than for the larger follower. This result is restricted to low Reynolds number cases, because of differences in viscous diffusion at higher Reynolds numbers. The crosswind does not alter the rolling moment histories at the vortex cores significantly, within the simulation time interval in this study. Validation of this hazard estimation method, comparing simulations with experimental results, will be performed in future research.

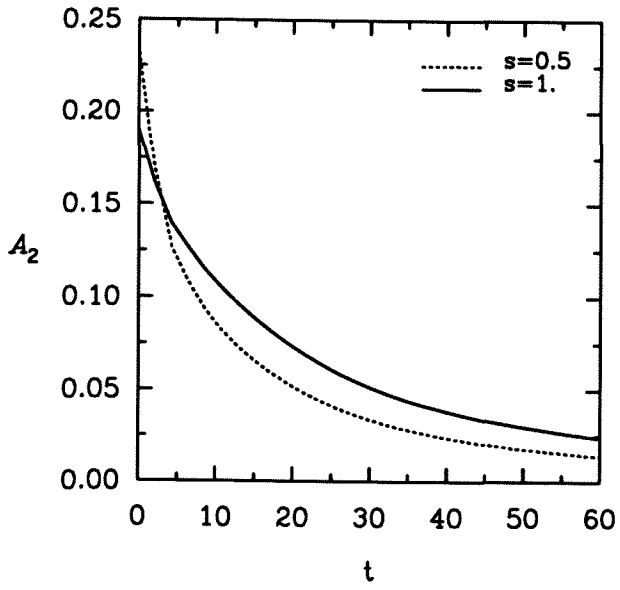

Figure 12 Rolling moment coefficient history at the left vortex center, with δ=10, U_∞ = 0.5

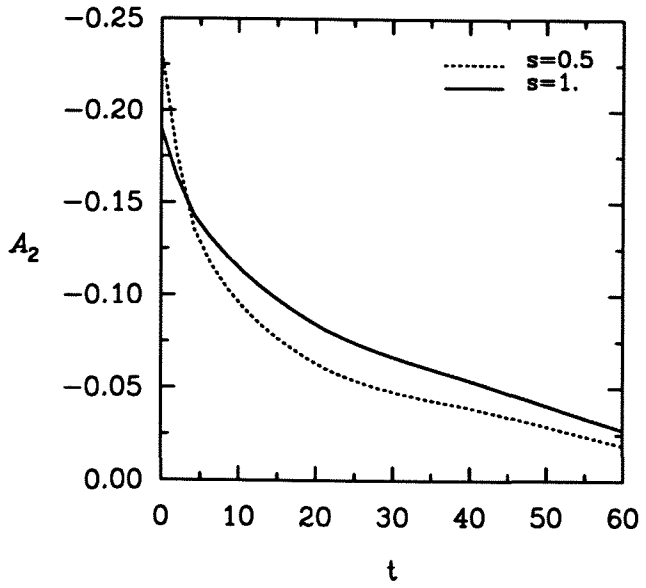

Figure 13 Rolling moment coefficient history at the right vortex center, with δ=10, U_∞ = 0.5

Acknowledgment

The first two authors would like to thank NASA Langley Research Center for the support of this work, under research grant NAG1–1437.

References

[1] Burnham, D. C., Hallock, J. N., Tombach, I. H., Brashears, M. R. and Barber, M. R. 1978 Ground based measurements of a B-747 aircraft in various configurations. U. S. Dept. of Transportation Report FAA-RD-78–146, December.

[2] Zheng, Z. and Ash, R. L. 1991 Viscous effects on a vortex wake in ground effect. *Proceedings of the Aircraft Wake Vortices Conference*, Vol II, pp 31–1 to 31–30, Washington, D.C., October 1991.

[3] Zheng, Z. and Ash, R. L. 1993 Prediction of turbulent wake vortex motion near the ground. *Transitional and Turbulent Compressible Flows*, L. D. Kral and T. A. Zang, eds., ASME Fluids Engineering Conference, FED Vol. 151, pp 195–207, Washington, D.C., June 1993.

[4] Liu, H. T. and Srnsky R. A. 1990 Laboratory investigation of atmospheric effects on vortex wakes. Flow Research Inc. Technical Report No. 497.

[5] Harvey, J. K. and Perry, F. J. 1971 Flowfield produced by trailing vortices in the vicinity of the ground. *AIAA J.* **9,** 1659–1660.

[6] Rossow, V. J. 1976 Convective merging of vortex cores in lift-generated wakes. AIAA 9th Fluid and Plasma Dynamics Conference, San Diego, Calif., AIAA Paper No. 76–415.

[7] Bilanin, A. J., Teske, M. E. and Hirsh, J. E. 1978 Neutral atmospheric effects on the dissipation of aircraft vortex wakes. *AIAA J.* **16**, 956–961.

[8] Donaldson, C. duP. and Bilanin, A. J. 1975 Vortex wakes of conventional aircraft. AGARDograph No. 204.

[9] Lissaman, P. B. S., Crow, S. C., MacCready, P. B., Jr., Tombach, I. H. and Bate, E. R., Jr. 1973 Aircraft vortex wake descent and decay under real atmospheric effects. Department of Transportation Report No. FAA-RD-73–120.

[10] Brashears, M. R., Logan, N. A. and Hallock, J. N. 1975 Effect of wind shear and ground plane on aircraft wake vortices. *J. Aircraft* **12**, 830–833.

[11] Delisi, D. P., Robins, R. E. and Fraser, R. B. 1987 The effects of stratification and wind shear on the evolution of aircraft wake vortices near the ground: Phase I Results. Northwest Research Associates, Inc. NWRA-87-R006.

[12] Speziale, C. G. 1986 On the advantages of the vorticity-velocity formulation of the equations of fluid dynamics. NASA Contractor Report 178125, ICASE Report No. 86–35.

[13] Swarztrauber, P. N. and Sweet, R. A. 1979 Algorithm 541, Efficient FORTRAN subprograms for the solution of separable elliptic partial differential equations [D3]. *ACM Trans. on Math. Software* **5**, 352–364.

[14] Lee, X. and Black, T. A. 1993 Atmospheric turbulence within and above a Douglas-Fir stand. Part I:

Statistical properties of the velocity field. *Boundary-Layer Meteorology* **64**, 149–174.

[15] Stewart, E. C. 1993 A study of the interaction between a wake vortex and an encountering airplane. AIAA Paper No. 93–3642, 1993 Atmospheric Flight Mechanics Conference, Monterey, California, August 9–11, 1993.

[16] Karamcheti, K. 1964 *Principles of Ideal-Fluid Aerodynamics*, Robert E. Krieger Publishing Company, Malabar, Florida

[17] Bertin, J. J. and Smith, M. L. 1979 *Aerodynamics for Engineers*, Prentice Hall, Englewood, New Jersey 07632

[18] Rossow, V. J. 1994 Validation of vortex-lattice method for loads on wings in lift-generated wakes. AIAA Paper 94–1839, AIAA 12th Applied Aerodynamics Conference, Colorado Springs, Co., June 20–23, 1994.